Edinburgh Research Explorer

Cost-Effective Quasi-Parallel Sensing Instrumentation for Industrial Chemical Species Tomography

Cost-Effective Quasi-Parallel Sensing Instrumentation for Industrial Chemical Species Tomography

Godwin Enemali, *Member, IEEE*, Rui Zhang, Hugh McCann, Chang Liu*, *Member, IEEE*

Abstract—Chemical Species Tomography (CST) has been widely applied for imaging of critical gas-phase parameters in industrial processes. To acquire high-fidelity images, CST is typically implemented by line-of-sight Wavelength Modulation Spectroscopy (WMS) measurements from multiple laser beams. In this work, we present a quasi-parallel sensing technique and electronic circuits for industrial CST that facilitates cost-effective implementation of industrial CST with very low complexity and reduced load on data transfer compared to the fully parallel sensing technique. Although the acquisition and processing of these multiple beams using a fully parallel data acquisition (DAQ) and signal processing system can achieve maximised temporal response in CST, it leads to a highly complex and power-consuming instrumentation with electronics-caused inconsistency between the sampled beams, in addition to significant burden on data transfer infrastructure. To address these issues, the digitisation and demodulation of the multi-beam signals in the proposed quasi-parallel sensing technique are multiplexed over the high-frequency modulation within a wavelength scan. Our development not only maintains the temporal response of the fully parallel sensing scheme, but also facilitates the cost-effective implementation of industrial CST with very low complexity and reduced load on data transfer. The proposed technique was analytically proofed and then numerically examined by noise-contaminated CST simulations. Finally, the designed electronics was experimentally validated using a lab-scale CST system with 32 laser beams.

Index Terms — Chemical Species Tomography (CST), Wavelength Modulation Spectroscopy (WMS), quasi-parallel, data acquisition, digital lock-in, instrumentation.

I. INTRODUCTION

INDUSTRIAL Process Tomography (IPT) has been widely applied to image, qualitatively and/or quantitatively, the behaviour of flows within processes in a non-intrusive manner. Various sensing modalities have been used, e.g. electrical tomography [1, 2], electromagnetic tomography [3], ultrasonic tomography [4, 5], x/γ-ray tomography [6], optical tomography [7], etc. Among these modalities, optical tomography utilising chemical species-dependent photon absorption is named Chemical Species Tomography (CST). Tunable diode laser absorption spectroscopy (TDLAS) is used in CST in a manner analogous to x-ray tomography, with the difference that, for incident light at an appropriately selected wavelength, the absorption measurements enable the reconstruction of the unknown spatial distribution of concentration of the target molecule [8]. Facilitated by the rapid technology development of the telecommunications industry, the last decade has witnessed accelerating advancement in the application of CST to solve industrial process engineering problems, e.g. vapour fuel imaging in internal combustion engines [9, 10], gas turbine exhaust imaging [11, 12], and power-plant boiler pollutant diagnosis [13].

Industrial CST is commonly implemented in harsh environments, suffering from significant noise in the line-of-sight (LoS) TDLAS measurements [14-16], dozens of which are required in order to achieve adequate spatial resolution [17]. The major sources of noise include electronic noise, optical noise, and environmental noise [18, 19]. To achieve better noise rejection capability, Calibration-Free Wavelength Modulation Spectroscopy (CF-WMS) is extensively adopted for implementing the LoS-TDLAS measurements in CST [20-24]. As shown in Fig. 1 (a), a high-frequency modulation (typically 40 kHz – 250 kHz) is added to a low-frequency wavelength scan (typically 1 Hz – 10 kHz). The CF-WMS scheme raises the signal detection band to a designated frequency range and then extracts the n-th harmonic signal by a demodulation process. Finally, path integrated absorbances for all the laser beams are calculated from the first harmonic normalised n-th harmonic signal, i.e. WMS-nf/$1f$. In most cases, WMS-$2f$/$1f$ is favoured due to its stronger intensity.

The hardware implementation of a data acquisition (DAQ) system for CF-WMS requires three basic elements: (a) high-speed digitisation by an analogue-to-digital converter (ADC) with adequate bandwidth for sampling the WMS-$2f$, (b) digital lock-in (DLI) module for simultaneous demodulation of WMS-

G. Enemali, R. Zhang, H. McCann and C. Liu are with the School of Engineering, University of Edinburgh, Edinburgh, EH9 3JL, U.K. (e-mail: C.Liu@ed.ac.uk)

2*f* and WMS-1*f*, and (c) real-time transferring of the sampled data to high-level processors for continuous image reconstruction. To date, there are two typical sensing schemes to implement the CF-WMS method on all the laser beams for CST, i.e. fully-parallel (FP) [11, 25] and time-division-multiplexing (TDM) [15, 26] sensing schemes.

As shown in Fig. 1 (b), the FP sensing scheme detects simultaneously the laser transmission signals for all the laser beams by introducing an ADC and a DLI module for each beam. Although the FP sensing scheme can maximise the temporal resolution of the CST, its hardware implementation will inevitably lead to a highly complex, power-consuming and expensive instrumentation system. Considering a CST system, typically, with more than 30 laser beams, the large number of signal amplifiers and ADCs inevitably cause some inconsistency between the sampled beams. In addition, the huge amount of spectral data sampled in parallel significantly burdens the data transfer in industrial applications [11], in which *in situ* signal digitisation is generally located remotely from the high-level processors. In case of on-board data storage, the sampled data will occupy the memory in a short period and thus hinder uninterrupted measurement.

Alternatively, the TDM sensing scheme shown in Fig. 1 (c) simplifies the hardware by multiplexing the laser beams on the intervals of the neighbouring wavelength scans. The selected laser beam with its transmission signal is digitised by the ADC and then demodulated. However, the temporal resolution of such a CST system is degraded by the sequential sampling. In the case of turbulent flow imaging, the TDM scheme will potentially lead to insufficient characterisation of the instantaneous chemical reactions and heat transfer.

To address the above-mentioned challenges, we present here a quasi-parallel (QP) sensing technique and electronic circuits for industrial CST. The QP scheme is achieved by multiplexing the multi-beam signals over the high-frequency modulation within a wavelength scan, enabling the digitisation and demodulation of these beams with a single ADC and a single DLI module. The QP sensing scheme, initially addressed in [27], not only maintains the temporal response of the FP

Figure 1: (a) Overview of a CST system with (b) Fully Parallel-DAQ sensing scheme, and (c) Time-Division Multiplexed-DAQ sensing scheme.

scheme, but also facilitates the cost-effective implementation of industrial CST with very low complexity and reduced load on data transfer. In this paper, we first illustrate the concept of the proposed scheme analytically. Then, numerical simulations are given, to examine the performance of the proposed scheme with noise-contaminated CST measurements. With electronic circuits designed to utilise a commercial off-the-shelf Field-Programmable Gate Array (FPGA) platform, the QP sensing scheme was experimentally validated using a lab-scale CST system with 32 laser beams.

II. METHODOLOGY

A. Background of WMS

The fundamentals of CF-WMS have been well developed for noise-resistant gas measurement [20, 21]. To facilitate our presentation of the proposed WMS-based QP sensing scheme, the critical equations in terms of laser intensity modulation and frequency modulation in CF-WMS are reviewed. The time-varying diode laser output intensity $I_0(t)$ can be expressed as

$$I_0(t) = I_{0,s}(t) + I_{0,m}(t) \tag{1}$$

where the components $I_{0,s}(t)$ and $I_{0,m}(t)$ reflect, respectively, the injection current scan and current modulation at frequencies f_s and f_m, given by Eqns. (2) and (3)where the same subscripts, s and m, are used for the corresponding scan and modulation currents, i_s and i_m.

$$I_{0,s}(t) = \bar{I}_0 \left[\tfrac{1}{2} + i_{1,s} cos\left(2\pi f_s t + \phi_{1,s}\right) + i_{2,s} cos\left(4\pi f_s t + \phi_{2,s}\right) \right] \tag{2}$$

$$I_{0,m}(t) = \bar{I}_0 \left[\tfrac{1}{2} + i_{1,m} cos\left(2\pi f_m t + \phi_{1,m}\right) + i_{2,m} cos\left(4\pi f_m t + \phi_{2,m}\right) \right] \tag{3}$$

where $\bar{I}_0$ [V] is the average laser intensity, i_1 and i_2 are the amplitudes of the first- and second-order laser intensity modulation, respectively, and ϕ_1 and ϕ_2 are the phase shifts between the intensity modulation and frequency modulation for linear and non-linear components, respectively. Note that in Eq. (1), I_0 is counted twice, therefore, a factor of ½ has been introduced in Eqs. (2) and (3) [21].

Accompanied by the intensity modulation, the output optical frequency of the laser, $v(t)$, can be modelled by

$$v(t) = \bar{v} + v_s(t) + v_m(t) \tag{4}$$

where $\bar{v}$ is the centre frequency, and $v_s(t)$ and $v_m(t)$ are the scanned and modulated frequencies, respectively. Similarly to $I_{0,s}(t)$ and $I_{0,m}(t)$, we express $v_s(t)$ and $v_m(t)$ as

$$v_s(t) = a_{1,s} cos\left(2\pi f_s t + \psi_{1,s}\right) + a_{2,s} cos(4\pi f_s t + \psi_{2,s}) \tag{5}$$

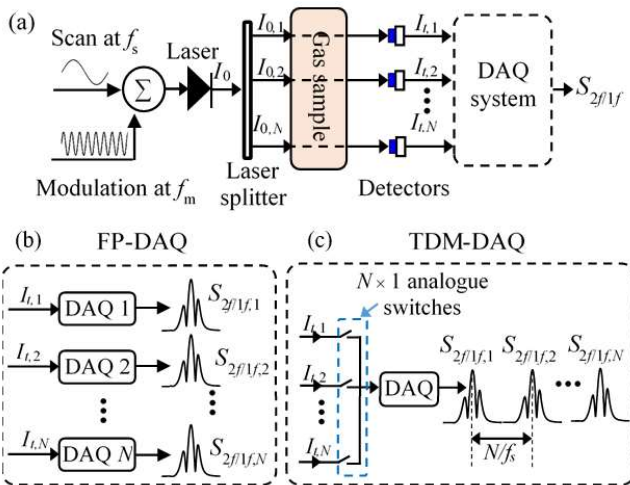$$v_m(t) = a_{1,m} cos\left(2\pi f_m t + \psi_{1,m}\right) + a_{2,m} cos(4\pi f_m t + \psi_{2,m}) \tag{6}$$

where a_1 and a_2 [cm^{-1}] are, respectively, first- and second-order amplitudes and again the subscripts s and m refer to scan and modulation, respectively. ψ_1 and ψ_2 are the first- and second-order phase shifts, respectively.

As shown in Fig. 1, the laser source is split into N beams which pass through the target gas sample. Denoting the absorbance of the i-th laser beam by $\alpha_i(v(t))$ ($i = 1, 2, \ldots, N$), the relationship between its incident intensity $I_{0,i}(t)$ and transmitted intensity $I_{t,i}(t)$ follows Beer-Lambert's law and can be expressed by

$$I_{t,i}(t) = I_{0,i}(t)e^{-\alpha_i(v(t))} \qquad (7)$$

Assuming, for the purpose of illustrating the basic sensing requirement, that the gas properties are uniform along each laser beam, $\alpha_i(v(t))$ can be calculated by

$$\alpha_i(v(t)) = L_i \phi(v(t)) P_i S(T_i) X_i \qquad (8)$$

where L_i [cm] is the path length of the i-th laser beam through the subject, $\phi(v)$ [cm] is the line-shape function, P_i [atm], X_i, and T_i [K] are the pressure, molar fraction of the absorbing species, and temperature, respectively, and $S(T)$ [cm^{-2}atm^{-1}] is the line strength of the selected absorption line. In CST, it is typical that X and T, and sometimes P, vary with position within the subject, and the aim of the technique is to recover the spatial distribution of X and/or T. In this work, the spectral data has been obtained from HITRAN2016 [28].

B. WMS-based QP Sensing Scheme for CST

As shown in Fig. 2, $I_{t,i}(t)$ from multiple beams are multiplexed within the wavelength scan at the resolution of the modulation period in the proposed QP sensing scheme. As a result, the multiplexed transmission signal, $I_{t,mux}(t)$ sampled by a single ADC and further processed by a DLI module can be expressed as

$$I_{t,mux}(t) = I_{t,i}(t)\big|_{t=(j-1)\times c/f_m}^{t=j\times c/f_m}, \ (j = 1, 2, \ldots) \qquad (9)$$

where j is the index of the multiplexing operation, and c is the number of modulation periods sampled per beam. In our implementation, Eq. (9) is implemented by using a fast analog 4 x 1 multiplexer operating at c/f_m between neighbouring beams. The index of laser beam being sampled, i, is calculated by

$$i = j - \lfloor (j-1)/N \rfloor \times N \qquad (10)$$

where N is the total number of beams multiplexed over a wavelength scan. The operand $\lfloor \bullet \rfloor$ is the floor function. For example, for 4 beams, and integer incrementing j in Eq. (10), we get $i = 1, 2, 3, 4, 1, 2, 3, 4, \ldots$. As a result, $I_{t,mux}(t)$ contains the intermittent $I_{t,i}(t)$ from all the N multiplexed laser beams within a wavelength scan. As the temporal resolution of a CST system depends on the frequency of the wavelength scan, the proposed QP sensing scheme can also maintain the maximum temporal resolution achieved using the FP sensing scheme, provided that all N beams are adequately sampled within a

single wavelength scan. Fig. 2 explicitly illustrates the QP sensing scheme for $c = 1$ and $N = 4$.

To achieve the CF-WMS scheme, the WMS-1f and WMS-2f signals are extracted from the digitised $I_{t,mux}(t)$, denoted as $I_{t,mux}(d)$, using the DLI module. The in-phase and quadrature components of the WMS-1f, $X_{1f,mux}$ and $Y_{1f,mux}$, and WMS-2f, $X_{2f,mux}$ and $Y_{2f,mux}$, can be obtained by [29]

$$X_{1f,mux} = \sum_{d=0}^{D-1} I_{t,mux}[d] \times R_{I,1f}[d] \qquad (11)$$

$$Y_{1f,mux} = \sum_{d=0}^{D-1} I_{t,mux}[d] \times R_{Q,1f}[d] \qquad (12)$$

$$X_{2f,mux} = \sum_{d=0}^{D-1} I_{t,mux}[d] \times R_{I,2f}[d] \qquad (13)$$

$$Y_{2f,mux} = \sum_{d=0}^{D-1} I_{t,mux}[d] \times R_{Q,2f}[d] \qquad (14)$$

where $R_{I,1f}[d]$ and $R_{Q,1f}[d]$ ($R_{I,2f}[d]$ and $R_{Q,2f}[d]$) are sinusoidal reference signals with $\pi/2$ difference in phase at f_m ($2f_m$), respectively. The total number of digitised samples $D = c \times \frac{f_d}{f_m}$, where f_d is the sampling frequency.

Similar to the demodulation of $I_{t,mux}(t)$, the non-absorbing background signal $I_{0,mux}(t)$ is sampled and demodulated to obtain the absorption-free in-phase and quadrature components, $X_{1f,mux}^0$, $Y_{1f,mux}^0$, $X_{2f,mux}^0$ and $Y_{2f,mux}^0$, respectively. The multiplexed, background subtracted, WMS-2f/1f signal, $^{mux}S_{2f/1f}$, is calculated as [22],

$$^{mux}S_{2f/1f} = \frac{}{\sqrt{\left(\dfrac{X_{2f,mux}}{R_{1f,mux}} - \dfrac{X_{2f,mux}^0}{R_{1f,mux}^0}\right)^2 + \left(\dfrac{Y_{2f,mux}}{R_{1f,mux}} - \dfrac{Y_{2f,mux}^0}{R_{1f,mux}^0}\right)^2}} \qquad (15)$$

where

$$R_{1f,mux}^0 = \sqrt{\left(X_{1f,mux}^0\right)^2 + \left(Y_{1f,mux}^0\right)^2} \qquad (16)$$
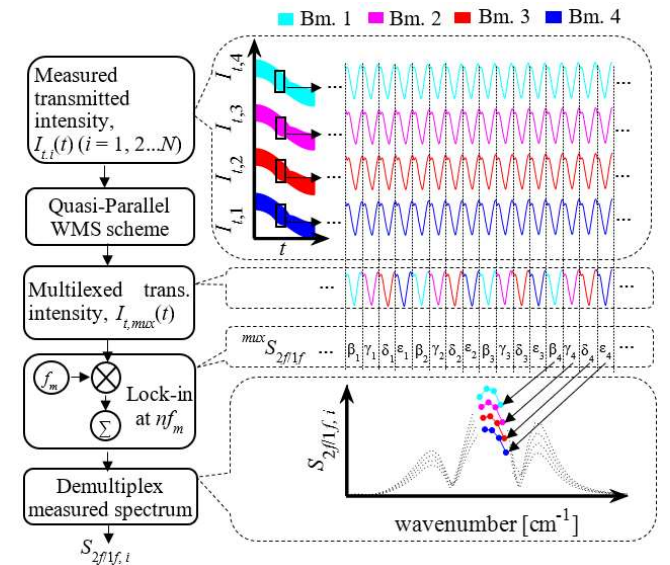

Figure 2: Flowchart of the QP-WMS sensing scheme demonstrated for four-beam multiplexing.

$$R_{1f,mux} = \sqrt{(X_{1f,mux})^2 + (Y_{1f,mux})^2} \qquad (17)$$

Each sample of $^{mux}S_{2f/1f}$ shown in Fig. 2 is demodulated from the accumulated c modulation periods. As a result, the samples of $^{mux}S_{2f/1f}$ from the multiplexed signal are obtained in sequence. For example, $^{mux}S_{2f/1f}$ obtained in Fig. 2 contains the samples from the 4 multiplexed beams and can be expressed as

$$^{mux}S_{2f/1f} = \{\dots \beta_1, \gamma_1, \delta_1, \varepsilon_1, \beta_2, \gamma_2, \delta_2, \varepsilon_2, \dots\}. \qquad (18)$$

where β_j, γ_j, δ_j, ε_j, denotes the samples of $^{mux}S_{2f/1f}$ obtained from the 4 multiplexed laser beams with the j-th multiplexing operation, respectively.

Then, the $^{mux}S_{2f/1f}$ is demultiplexed to recover the $S_{2f/1f}$ spectrum for each beam, $S_{2f/1f,i}$ ($i = 1, 2, 3, 4$), as

$$S_{2f/1f,1} = \{\dots \beta_1, \beta_2, \dots\} \qquad (19)$$

$$S_{2f/1f,2} = \{\dots \gamma_1, \gamma_2, \dots\} \qquad (20)$$

$$S_{2f/1f,3} = \{\dots \delta_1, \delta_2, \dots\} \qquad (21)$$

$$S_{2f/1f,4} = \{\dots \varepsilon_1, \varepsilon_2, \dots\} \qquad (22)$$

It is worth mentioning that the Multiply and Accumulate (MAC) filter (Eqs. 11 – 14) is better suited for discontinuously sampled signal such as those resulting from the proposed QP scheme compared to FFT method or other common filtering techniques such as the Infinite Impulse Response (IIR) filters. MAC filters can operate at the resolution of the modulation frequency. Therefore, a single MAC filter can be switched between different beams in runtime, unlike the FFT and IIR filters which rely on continuous signals.

III. NUMERICAL SIMULATION

A. Simulation Set up

Numerical simulation was carried out to validate the proposed QP sensing scheme using the water absorption transition at 7185.6 cm^{-1}. Four laser beams were used in the simulation. Along the laser path with length of 36 cm, temperature and pressure were assumed to be uniform at 293 K and 1 atm, respectively. The water concentrations on the four laser paths were assumed to be 0.8% (mole fraction), 0.7%, 0.6% and 0.5%, respectively. The water is vapour mixed with air. f_s and f_m were set to 31.25 Hz and 62.5 kHz respectively, i.e. f_m was 2,000 times f_s, ensuring that all beams could be sampled many times during the wavelength scan. $a_{1,s}, a_{1,m}, \bar{I}_0, i_{1,s}, i_{1,m}$ were set as 0.25 [cm^{-1}], 0.006 [cm^{-1}], 0.5 [V], 0.2 and 0.1 respectively. As the absorption feature is scanned twice within each sinusoidal scan, only the falling part of the scan is used in this work, as shown in Fig. 3. According to Eqn. (9), the transmission signals, $I_{t,i}(t)$ ($i = 1, 2, 3, 4$), were multiplexed to obtain $I_{t,mux}(t)$. By following the similar procedures, $I_{0,mux}(t)$ was also obtained. Both $I_{t,mux}(t)$ and $I_{0,mux}(t)$ were digitised at a rate of f_d = 15.625 Mega Samples per second (MSps) with a single ADC and subsequently demodulated by a DLI module with c = 2 to obtain $^{mux}S_{2f/1f}$.

As shown in Fig. 4 (a), the demodulated $^{mux}S_{2f/1f}$ contains 500 samples on the wavelength. Using Eqns. (18) to (22),

$S_{2f/1f,i}$ ($i = 1, 2, 3, 4$), each with 125 samples shown in Fig. 4 (b), is obtained after the demultiplexing. The harmonic information for the four beams can be obtained using a single ADC-DLI pair with a sampling interval of 32 μs ($4/f_m/c$) between the neighbouring beams. Therefore, the temporal response of the QP sensing scheme is much superior to the TDM scheme that samples the neighbouring beams with a sampling interval of 32 ms ($1/f_s$) with the same settings. In comparison with the FP sensing scheme, the proposed QP scheme saves 75% hardware resources in terms of both the ADC-DLI pairs and memory space, whilst maintaining the frame rate of the CST system, i.e. f_s. The reduced data throughput also alleviates the requirement placed on bandwidth, thus facilitating remote data transfer in real time.

The QP scheme is superior to the TDM scheme not only by achieving a better temporal resolution, but also in minimizing the sampling interval between neighbouring beams. Table I shows a comparison between FP, TDM and the proposed QP schemes in terms of temporal resolution and sampling interval between neighbouring beams for scan frequencies fs of 31.25 Hz and 125 Hz (keeping modulation frequency, f_m, at 62.5 kHz). It can be seen that the temporal resolution of QP scheme, like that of the FP scheme, will always be 4 times that of the TDM. Furthermore, the sampling interval of the QP scheme for neighbouring beams is significantly less than the TDM,
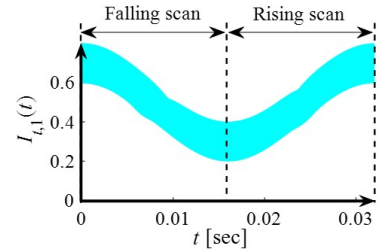

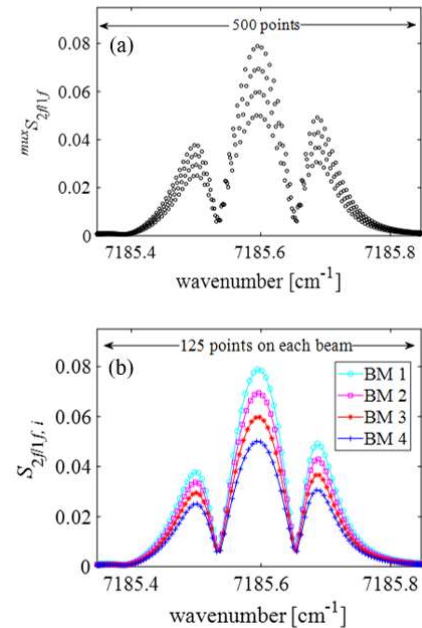Figure 3: Simulated raw transmitted signal for beam 1.

Figure 4. For the four-beam simulated sensing using QP-WMS, (a) the demodulated $^{mux}S_{2f/1f}$ and (b) the demultiplexed $S_{2f/1f,i}$.

indicating its stronger representativeness of a FP system.

B. Numerical Results and Discussions

The performance of the proposed QP sensing scheme is examined by considering the practical measurements, in which the transmission for each laser beam is contaminated by various forms of noise. The sources of noise can be characterised by frequency-dependent noise and frequency-independent noise, respectively. The frequency-dependent noise mainly contains pink noise ($1/f$ noise), e.g. laser and detector excess noise, and low-frequency environmental noise generally caused by background scattering and flow-induced beam steering. The frequency-independent noise, which is known to have a white noise spectrum, is dominated by the thermal noise from the detector, signal amplification and digitisation circuits [18]. In the simulation, the Signal-to-Noise Ratio (SNR) for the environmental noise was set to 15 dB lower, with respect to I_t. As shown in Fig. 5, this noise level was quantified by measuring the laser intensity fluctuation when a turbulent heated flow was imposed on a laser beam with stable intensity. To be specific, both the noise-free signal (without the turbulence) and the noise-contaminated signal (with the turbulence) were measured with the Red Pitaya ADC with a bandwidth of 40 MHz. Then, these signals were inputted into the MATLAB *snr* function to estimate the environmental noise. In addition, the combined pink and white noise was set to 56 dB lower with respect to I_t in the simulation. As shown in Table II, being calculated at the frequency of 62.5 kHz, consistent with the modulation frequency, this noise level can be justified by the noise

performance of the major components in the detection system that will be detailed in Section IV. From noise figures quoted in the datasheet of the components listed, we computed the dB level used in the simulations.

Fig. 6 shows a flowchart of the simulated implementation of the QP sensing scheme with sequentially imposed multiple sources of noise. The three types of noise used in our work are all additive noise. As the low-frequency environmental noise is introduced during beam propagation, it is firstly added to the noise-free transmission for the i-th beam. Subsequently, the pink noise and white noise, mainly introduced by the detector and data acquisition (DAQ), are added, resulting in the noise-contaminated transmission, $I_{t,i}(t)$. Finally, the multi-beam transmission signals are multiplexed and demodulated to obtain the $S_{2f/1f,i}$, from which the path integrated absorbances can be obtained for image reconstruction [30].

To be specific, Fig. 7 (a-d) demonstrates the noise-contaminated transmission signals for the four beams noted above in Section III A. All the three sources of noise were randomly generated within Gaussian distributions with zero mean and standard deviation set to the fixed noise levels, i.e. 15 dB for environmental noise, and 56 dB for pink and white noise. To validate the proposed scheme, $I_{t,i}(t)$ ($i = 1, 2, 3, 4$) were

TABLE I
COMPARISON OF THE TEMPORAL RESOLUTION AND SAMPLING INTERVAL AMONG DIFFERENT DAQ SCHEMES.

Sensing schemes	Temporal Resolution (frames per second, fps)		Sampling interval	
	f_s = 31.25 Hz	f_s = 125 Hz	f_s = 31.25 Hz	f_s = 125 Hz
TDM	31.25/4	31.25	32 ms	8 ms
FP	31.25	125	-	-
QP	31.25	125	32 µs	32 µs

TABLE II
NOISE PERFORMANCE OF MAJOR COMPONENTS

Photo-detector (G12182-003K, Hamamatsu)	Pre-amp (AD8033, Analog Devices)	Mux (ADG704, Analog Devices)	PGA (THS7002, Texas Instruments)	Red Pitaya
6.5e-13 W/√Hz	11 nV/√Hz	82dB*	1.7 nV/√Hz	71.3 dB

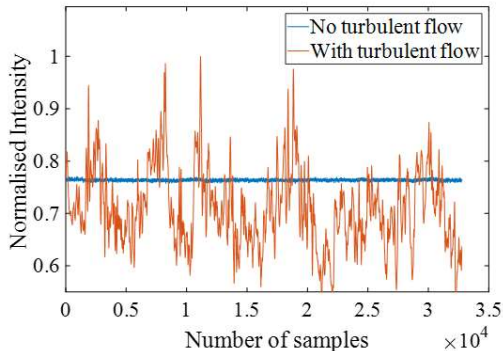* due cross talk noted in the datasheet

Figure 5: Quantification of laser intensity fluctuations when a turbulent heated flow was imposed on a laser beam with stable intensity. The measurements were taken at 15.625 MSps

TABLE III
COMPARISON OF FITTING RESIDUALS BETWEEN FP AND QP SCHEME

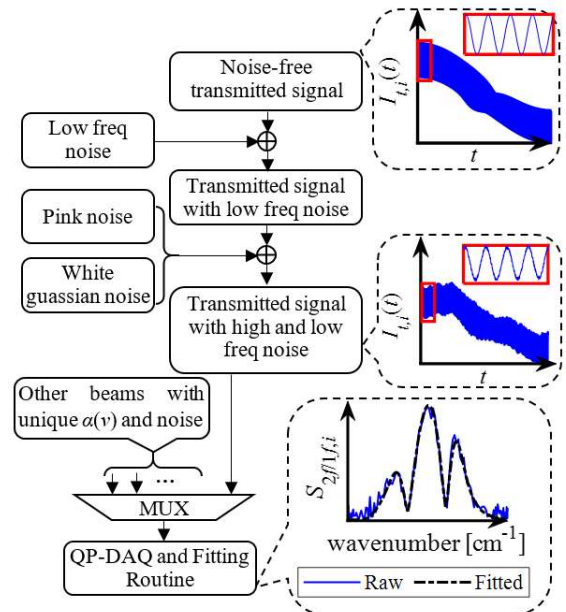| Beam	Parameter	FP	QP	Difference (%)
BM 1	Mean (10^{-3})	6.2017	6.1988	0.0468
	Std. (10^{-4})	2.3082	2.3046	0.1560
BM 2	Mean (10^{-3})	5.5534	5.5310	0.4034
	Std. (10^{-4})	3.5778	3.5157	1.7357
BM 3	Mean (10^{-3})	4.8518	4.8280	0.4905
	Std. (10^{-4})	3.4364	3.4686	0.9370
BM 4	Mean (10^{-3})	4.1496	4.1264	0.5591
	Std. (10^{-4})	3.5033	3.4365	1.9068

Figure 6: Flowchart of the simulated implementation of the QP sensing scheme with sequentially introduced multiple sources of noise.

demodulated and fitted by using both the QP and FP sensing schemes. As shown in Figs. 7 (e-h) and (i-l), the proposed QP scheme, with only one quarter of the total number of samples in comparison with the FP sensing scheme, yields fitting results with similar residuals. To be quantitative and statistical, Table III shows the mean and standard deviation (std.) of the residual difference between the demodulated and fitted $S_{2f/1f,i}$ data for both the FP and QP sensing schemes using 500 repetitive simulations. Both the mean and std. values are very similar for both schemes with a maximum difference of 0.56% and 1.91%, respectively.

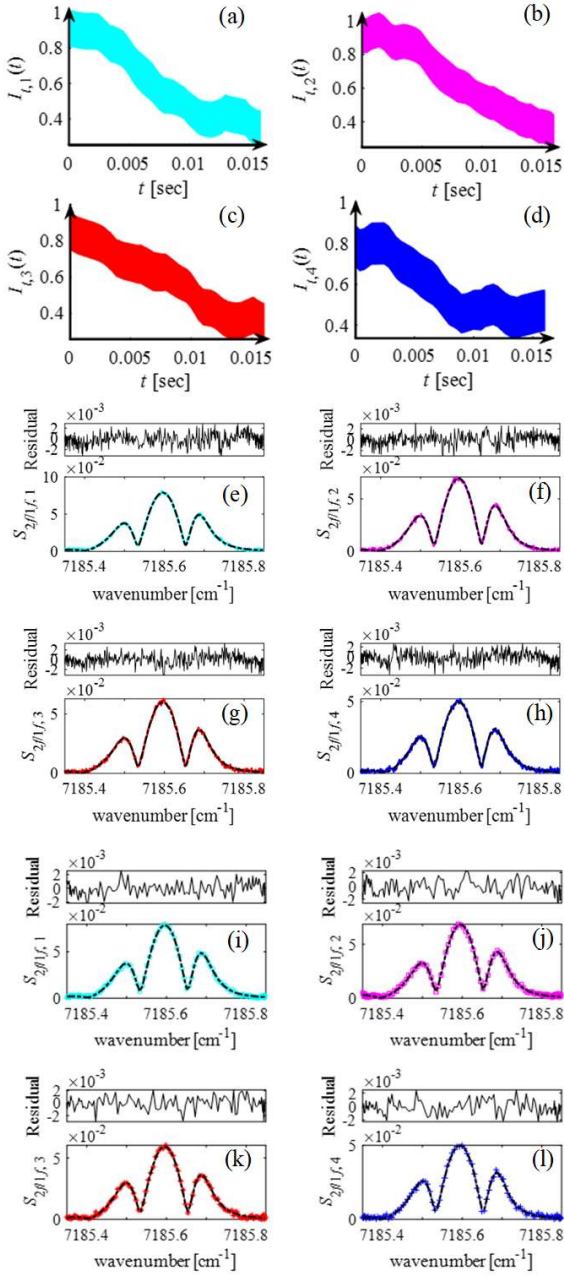In comparison with the FP sensing scheme, the proposed QP

Figure 7. Implementation of both the FP and QP sensing schemes on the same laser transmission signals. (a-d) shows the simulated noise-contaminated transmission signals for the four laser beams. (e-h) and (i-l) shows the demodulated and fitted $S_{2f/1f,i}$ using the FP and QP sensing schemes, respectively.

scheme only generates one quarter of the total number of samples, i.e. 500 samples per scan in FP vs 125 samples per scan in QP. However, the noise introduced by lower Nyquist frequency in the QP scheme can be mitigated by the spectral fitting process, yields fitting results with similar residuals shown in Figs. 7 (e-h) and (i-l).

IV. HARDWARE AND FIRMWARE IMPLEMENTATION

For hardware implementation of the QP sensing scheme, we designed a signal conditioning circuit (SCC), which consists of (a) a 4-to-1 multiplexer (ADG704, Analogue Devices) to produce the multiplexed transmission signal, $I_{t,mux}(t)$, from the four laser beams, and (b) a programmable gain amplifier (PGA) (THS7002, Texas Instruments) that further conditions the multiplexed signal. As shown in Fig. 8 (a), the control bits for the SCC are derived from the digital inputs/outputs (DIOs) on a commercial off-the-shelf FPGA platform, the Red Pitaya (RP) [31]. We used the STEMlab 125-14 kit. For more detailed specifications of STEMlab 125-14, please refer to [31]. The analogue output from the SCC is digitised by a 14-bit 125 MSps ADC that is integral to the RP.

The worst-case response time, t_{mux}, of the ADG704 is 33 ns. To guarantee signal integrity, t_{mux} must satisfy

$$t_{mux} < 1/f_d. \quad (23)$$

That is to say, the multiplexed signal must be stabilised between the neighbouring samples digitised by the ADC. As a result, the theoretical maximum sampling frequency f_d supported in the design is 30.3 MHz. Its switching control is implemented by a multiplexer switching timing control (MSTC) logic. The MSTC synchronises the switching operation of the multiplexer to the ADC by taking c, f_d, and f_m into account, generating precisely
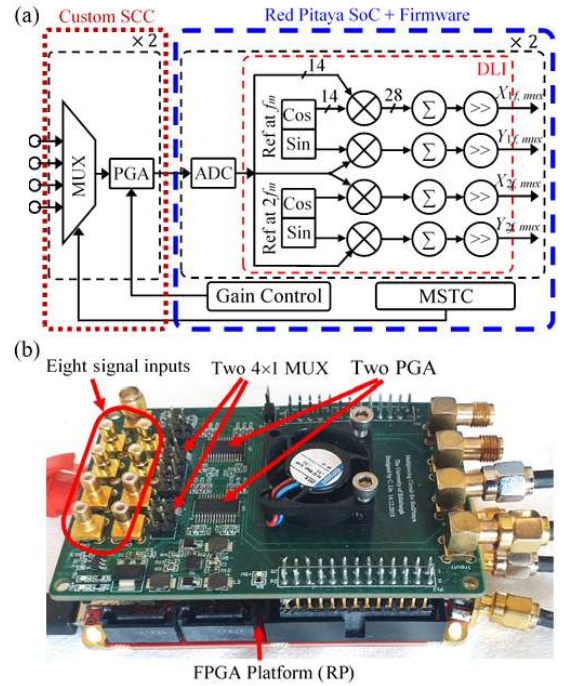

Figure 8: Hardware implementation of QP sensing scheme: (a) schematics of the SCC and the FPGA platform; (b) photograph of the hardware circuits, indicating the layout.

timed logic signals that select the laser beam to be sampled per modulation period.

Subsequently, the digitised $I_{t,mux}(t)$ is demodulated by the DLI customised on the FPGA (Xilinx 7 series ZYNQ 7010) of the RP at the frequencies of $1f_m$ and $2f_m$. For each frequency, two 14-bit sinusoidal reference signals with phase difference of 90 degrees are generated using Xilinx's DDS IPs and then multiplied by the 14-bit digitised $I_{t,mux}(t)$. According to Eqns. (11)-(14), the quadrature components, $X_{1f,mux}$ and $Y_{1f,mux}$, $X_{2f,mux}$ and $Y_{2f,mux}$, can be obtained by accumulating the 28-bit multiplied signals for c modulation periods. The accumulation process increases each quadrature component to $[28 + log(c * f_s/f_m)]$ bits. As a standard 32-bit embedded processor is used for data post-processing and transfer, shift operation, as shown in Fig. 8 (a), is adopted to discard excess less significant bits. As a result, overflow can be avoided while maintaining minimal loss in precision. Finally, the quadrature components are transferred to the PC via Ethernet protocol.

As each RP is equipped with two simultaneous ADCs, the developed SCC and the DLI firmware are also duplicated, enabling two sets of 4-beam QP sensing. Fig. 8 (b) shows the hardware circuits, which enable a very compact implementation. The FPGA resources incurred by the QP sensing scheme in addition to the base firmware of RP are 1334 Flip Flops, 1456 Look-up Tables, 19 Block RAMs and 8 DSPs.

V. EXPERIMENTS

A. Experimental Set Up

To experimentally validate the proposed QP sensing system, a CST system with 32 laser beams was developed to image the two-dimensional (2D) distribution of water vapour (H_2O) concentration. As each measurement hub (Fig. 9(a)) is capable of measuring 8 beams with the QP sensing scheme, as discussed above and shown in Fig. 8, four hubs were utilised. A distributed feedback laser diode (NLK1E5GAAA, NTT Electronics) working at 7185.6 cm^{-1} was used for H_2O sensing in the experiment reported here. The laser was fed with a signal consisting of a scan sinusoid at f_s = 31.25 Hz and modulation sinusoid at f_m = 62.5 kHz from an arbitrary signal generator (ASG). Using a 32-way fibre splitter, the output laser from the pigtailed laser diode was equally split into 32 channels, each collimated by a fibre collimator (CFC5-C, Thorlabs) for launch across the subject. As shown in Fig. 9 (a), the 32 laser beams were arranged in 4 equiangular projections (45°) with 8 parallel beams in each projection. The neighbouring beam spacing, d, is 1.8 cm, while the distance D between the emitter and detector of each beam is 36.76 cm. Each transmitted laser beam was incident on a dedicated photodetector (G12182-003K, Hamamatsu). The 32 transmission signals were processed in QP mode, with a dedicated hub for each group of 8 signals, multiplexing 4 signals to each ADC, sampling at 15.625 MSps. With $c = 2$, a total of 500 samples were accumulated for each DLI operation to obtain 1000 wavelength samples in $^{mux}S_{2f/1f}$ per frame on each hub. Finally, signals were demultiplexed to obtain $S_{2f/1f,i}$ for all 32 beams, leading to 125 wavelength points in falling and rising part of the scan, respectively. The data acquisition was synchronised to the laser driver by means of a trigger generated by the ASG at f_s. Data

transfer to a remote PC from the 4 hubs was achieved using an Ethernet switch (GO-SW-5G, D-Link), enabling transfer of 4000×32 bits per hub per frame. The tomographic frame rate was 31.25 fps.

B. Experimental Results and Discussion

To examine the noise performance of the developed electronics, the $S_{2f/1f,i}$ ($i = 1,2,3,4$) were measured using a single DAQ channel for 100 times in room air without any artificially generated H_2O absorption. Mole fraction of water was 0.0135. In this case, there is no flow-induced uncertainty imposed on the laser beams. As shown in Fig. 10, each $S_{2f/1f,i}$ contains 125 wavelength samples with the proposed QP sensing scheme. Fig. 10 shows the mean value of each $S_{2f/1f,i}$, while the error bars show the standard deviation. As the temperature, H_2O concentration and path length are same for the four laser beams, the peak values of the sampled $S_{2f/1f,i}$ ($i = 1,2,...,4$) are very close, with a maximum difference of 2.3%. The maximum standard deviation of
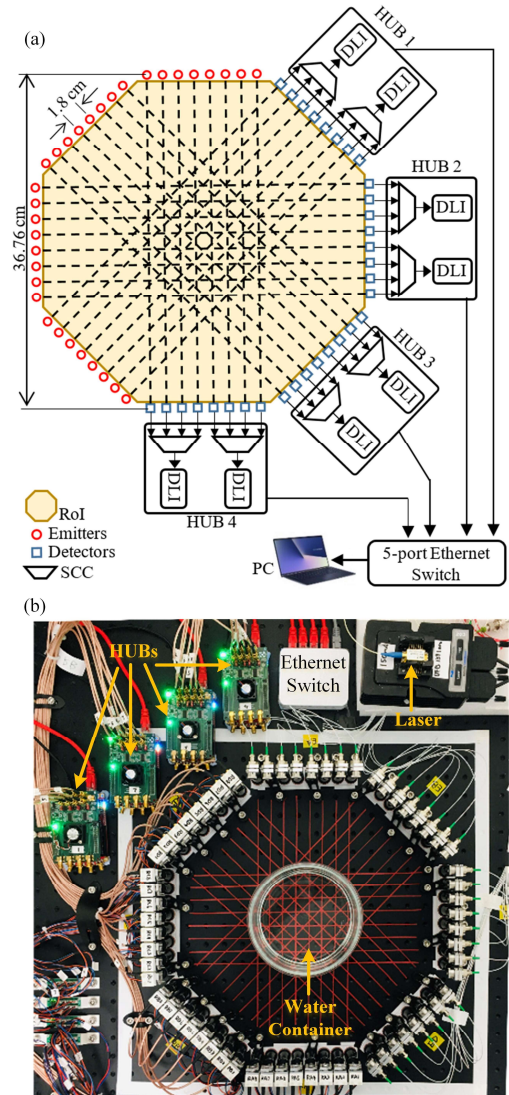

Figure 9: Hardware implementation of QP sensing scheme. (a) shows the schematic of SCC and the FPGA platform. (b) shows the picture of the hardware circuits.

$S_{2f/1f,i}$ observed for any of the four beams is 0.0052, demonstrating excellent noise suppression by the developed QP sensing instrumentation.

A phantom (i.e. known) 2D H_2O vapour distribution was generated using a container filled with hot water, and the measurement plane placed vertically above it, in a simple proof-of-concept experiment. As shown in Fig. 9 (b), the container was placed at the centre of the Region of Interest (RoI). Fig. 11 shows the sampled and fitted $S_{2f/1f,i}$ from the same four laser beams for a single frame of data. Stronger absorption can be observed for beams 3 and 4, due to their penetration of the evaporated H_2O with longer path length. To reconstruct the 2D distribution of H_2O concentration, the path integrated absorbances from the 32 laser beams were calculated from the fitting results.
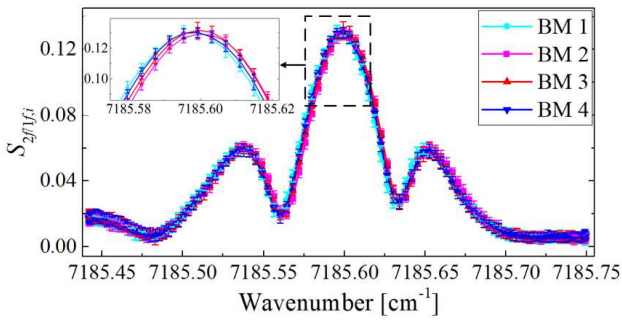

Figure 10: Repetitively measured $S_{2f/1f,i}$ ($i = 1, 2, 3, 4$) for 100 times using the developed QP sensing scheme and instrumentation on a single DAQ channel.
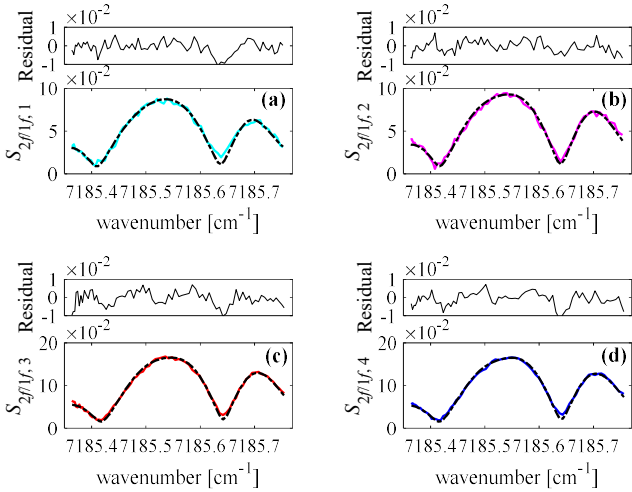

Figure 11: Spectral fitting of the experimental signals. (a-d) shows the demodulated and fitted $S_{2f/1f,i}$ from the same four laser beams for a single frame of data using the QP sensing schemes.
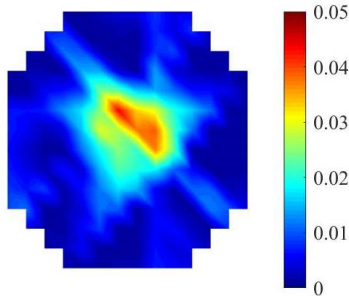

Figure 12: Reconstructed 2D distribution of H_2O concentration using the developed QP sensing scheme and instrumentation.

Fig. 12 shows the resulting image of H_2O concentration reconstructed using the Simultaneous Algebraic Reconstruction Technique (SART) with detailed procedures illustrated in our previous research [32]. The reconstructed image exhibits good quality with few artefacts, but also agrees well with the phantom in terms of the location of the high H_2O concentration region relative to room air. It is also worth mentioning that the image reconstruction in Fig. 12 demonstrates that the proposed QP sensing scheme, and the developed instrumentation, can be successfully applied to CST. The image reconstruction is influenced by many other factors, such as the constraints imposed on the inverse problem [33] and image reconstruction algorithms [34]. In our future work, we will incorporate the developed scheme and hardware to investigate the various constraints and image reconstruction algorithms.

VI. CONCLUSION

This paper introduces a cost-effective QP sensing technique and instrumentation scheme, developed for industrial application of CST. The new development implements, for the first time, multiplexing of multi-beam transmission signals over the high-frequency modulation within each wavelength scan, followed by digitisation and demodulation. Consequently, it significantly reduces the hardware/firmware complexity of CST implementation and its load on data transfer. In particular, this scheme enables a large number of laser beams to be employed in industrial systems robustly and cost-effectively.

The proposed technique was analytically demonstrated and then numerically examined by simulations. In the simulation, electronic, optical and environmental noise were added to the noise-free transmission signal. The $S_{2f/1f}$ was obtained using both the QP and FP sensing schemes, and fitted for quantitative comparison. The results show the proposed QP scheme saves three quarters of the wavelength samples in comparison with the FP sensing scheme, but with excellent fitting results with maximum differences of 0.56 % and 1.91 % in the mean and standard deviation of the fitting residuals.

Furthermore, electronic circuits were developed and a lab-scale CST system with 32 laser beams was set up to experimentally validate the proposed scheme. Experimental results further demonstrated that high-fidelity harmonic signals can be obtained using the proposed QP sensing scheme. Finally, the path integrated absorbances extracted from the harmonic signals were used to reconstruct a 2D distribution of H_2O concentration, demonstrating the effectiveness of the developed technique and instrument.

REFERENCES

[1] N. Borijindargoon, B. P. Ng, and S. Rahardja, "MUSIC-Like Algorithm for Source Localization in Electrical Impedance Tomography," *IEEE Transactions on Industrial Electronics,* vol. 66, pp. 4661-4671, 2019.

[2] M. Meribout and I. M. Saied, "Real-Time Two-Dimensional Imaging of Solid Contaminants in Gas Pipelines Using an Electrical Capacitance Tomography System," *IEEE Transactions on Industrial Electronics,* vol. 64, pp. 3989-3996, 2017.

[3] Z. Liu, W. Li, F. Xue, J. Xiafang, B. Bu, and Z. Yi, "Electromagnetic Tomography Rail Defect Inspection," *IEEE Transactions on Magnetics,* vol. 51, pp. 1-7, 2015.

[4] C. Tan, X. Li, H. Liu, and F. Dong, "An Ultrasonic Transmission/Reflection Tomography System for Industrial Multiphase

Flow Imaging," *IEEE Transactions on Industrial Electronics,* vol. 66, pp. 9539-9548, 2019.

[5] H. Liu, C. Tan, S. Zhao, and F. Dong, "Nonlinear Ultrasonic Transmissive Tomography for Low-Contrast Biphasic Medium Imaging Using Continuous-Wave Excitation," *IEEE Transactions on Industrial Electronics,* vol. 67, pp. 8878-8888, 2020.

[6] I. Kumpová, M. Vopálenský, T. Fíla, D. Kytýř, D. Vavřík, M. Pichotka*, et al.*, "On-the-Fly Fast X-Ray Tomography Using a CdTe Pixelated Detector—Application in Mechanical Testing," *IEEE Transactions on Nuclear Science,* vol. 65, pp. 2870-2876, 2018.

[7] J. Jamaludin, R. A. Rahim, M. H. F. Rahiman, and J. M. Rohani, "CCD Optical Tomography System to Detect Solid Contamination in Crystal-Clear Water," *IEEE Transactions on Industrial Electronics,* vol. 67, pp. 3248-3256, 2020.

[8] H. McCann, P. Wright, and K. Daun, "Chemical Species Tomography," in *Industrial Tomography: Systems and Applications*, M. Wang, Ed., Cambridge, UK: Woodhead Publishing, pp. 135-174, 2015.

[9] S. A. Tsekenis, D. Wilson, M. Lengden, J. Hyvönen, J. Leinonen, A. Shah*, et al.*, "Towards in-cylinder chemical species tomography on large-bore IC engines with pre-chamber," *Flow Measurement and Instrumentation,* vol. 53, pp. 116-125, 2017.

[10] N. Terzija, S. Karagiannopoulos, S. Begg, P. Wright, K. Ozanyan, and H. McCann, "Tomographic imaging of the liquid and vapour fuel distributions in a single-cylinder direct-injection gasoline engine," *International Journal of Engine Research,* vol. 16, pp. 565-579, 2015.

[11] E. M. D. Fisher, S. Tsekenis, Y. Yang, A. Chighine, C. Liu, N. Polydorides*, et al.*, "A Custom, High-Channel Count Data Acquisition System for Chemical Species Tomography of Aero-Jet Engine Exhaust Plumes," *IEEE Transactions on Instrumentation and Measurement,* vol. 69, pp. 549-558, 2020.

[12] T. Benoy, D. Wilson, M. Lengden, I. Armstrong, G. Stewart, and W. Johnstone, "Measurement of CO2 Concentration and Temperature in an Aero Engine Exhaust Plume Using Wavelength Modulation Spectroscopy," *IEEE Sensors Journal,* vol. 17, pp. 6409-6417, 2017.

[13] Y. Deguchi, T. Kamimoto, Z. Z. Wang, J. J. Yan, J. P. Liu, H. Watanabe*, et al.*, "Applications of laser diagnostics to thermal power plants and engines," *Applied Thermal Engineering,* vol. 73, pp. 1453-1464, 2014.

[14] C. Liu and L. Xu, "Laser absorption spectroscopy for combustion diagnosis in reactive flows: A review," *Applied Spectroscopy Reviews,* vol. 54, pp. 1-44, 2019.

[15] C. Liu, Z. Cao, Y. Lin, L. Xu, and H. McCann, "Online cross-sectional monitoring of a swirling flame using TDLAS tomography," *IEEE Transactions on Instrumentation and Measurement,* vol. 67, pp. 1338-1348, 2018.

[16] C. S. Goldenstein, R. M. Spearrin, J. B. Jeffries, and R. K. Hanson, "Infrared laser-absorption sensing for combustion gases," *Progress in Energy and Combustion Science,* vol. 60, pp. 132-176, 2017.

[17] C. Liu, S.-A. Tsekenis, N. Polydorides, and H. McCann, "Towards customized spatial resolution in TDLAS tomography", *IEEE Sensors J.*, vol. 19, pp. 1748-1755, 2019.

[18] Z. Wang, P. Fu, and X. Chao, "Laser Absorption Sensing Systems: Challenges, Modeling, and Design Optimization," *Applied Sciences,* vol. 9, p. 2723, 2019.

[19] L. M. Israa, T. A. Gary, and C. Youhua, "Noise estimation technique to reduce the effects of 1/f noise in Open Path Tunable Diode Laser Absorption Spectrometry (OP-TDLAS)," in *Proc.SPIE*, 2014.

[20] K. Sun, X. Chao, R. Sur, C. S. Goldenstein, J. B. Jeffries, and R. K. Hanson, "Analysis of calibration-free wavelength-scanned wavelength modulation spectroscopy for practical gas sensing using tunable diode lasers," *Measurement Science and Technology,* vol. 24, p. 125203, 2013.

[21] C. S. Goldenstein, C. L. Strand, I. A. Schultz, K. Sun, J. B. Jeffries, and R. K. Hanson, "Fitting of calibration-free scanned-wavelength-modulation spectroscopy spectra for determination of gas properties and absorption lineshapes," *Applied Optics,* vol. 53, pp. 356-367, 2014.

[22] G. B. Rieker, J. B. Jeffries, and R. K. Hanson, "Calibration-free wavelength-modulation spectroscopy for measurements of gas temperature and concentration in harsh environments," *Appl. Opt.,* vol. 48, pp. 5546-5560, 2009.

[23] A. J. McGettrick, K. Duffin, W. Johnstone, G. Stewart, and D. G. Moodie, "Tunable Diode Laser Spectroscopy With Wavelength Modulation: A Phasor Decomposition Method for Calibration-Free Measurements of Gas Concentration and Pressure," *Journal of Lightwave Technology,* vol. 26, no. 4, pp. 432-440, 2008.

[24] A. Upadhyay, D. Wilson, M. Lengden, A. L. Chakraborty, G. Stewart, and W. Johnstone, "Calibration-Free WMS Using a cw-DFB-QCL, a VCSEL, and an Edge-Emitting DFB Laser with In-Situ Real-Time Laser Parameter Characterization," *IEEE Photonics Journal,* vol. 9, no. 2, 2017.

[25] A. Huang, Z. Cao, W. Zhao, H. Zhang, and L. Xu, "Frequency Division Multiplexing and Main Peak Scanning WMS Method for TDLAS Tomography in Flame Monitoring," *IEEE Transactions on Instrumentation and Measurement,* vol. 69, pp. 9087-9096, 2020.

[26] L. Xu, C. Liu, W. Jing, Z. Cao, X. Xue, and Y. Lin, "Tunable diode laser absorption spectroscopy-based tomography system for on-line monitoring of two-dimensional distributions of temperature and H2O mole fraction," *Review of Scientific Instruments,* vol. 87, p. 013101, 2016.

[27] G. Enemali, C. Liu, N. Polydorides, and H. McCann, "A Quasi-Parallel DAQ Scheme for Wavelength Modulation Spectroscopy Tomography," in *2019 IEEE International Conference on Imaging Systems and Techniques (IST)*, pp. 1-5, 2019.

[28] I. E. Gordon, L. S. Rothman, C. Hill, R. V. Kochanov, Y. Tan, P. F. Bernath*, et al.*, "The HITRAN2016 molecular spectroscopic database," *Journal of Quantitative Spectroscopy and Radiative Transfer,* vol. 203, pp. 3-69, 2017.

[29] A. Chighine, E. Fisher, D. Wilson, M. Lengden, W. Johnstone, and H. McCann, "An FPGA-based lock-in detection system to enable Chemical Species Tomography using TDLAS," in *2015 IEEE International Conference on Imaging Systems and Techniques (IST)*, pp. 1-5, 2015.

[30] L. Xu, R. Xue, Y. Li, H. Zhang, and Z. Cao, "FPGA-Based Real-Time Implementation of Temperature Measurement via Tunable Diode Laser Absorption Spectroscopy," *IEEE Sensors Journal,* vol. 18, pp. 2751-2758, 2018.

[31] S. Red Pitaya d. d. *www.redpitaya.com*.

[32] Y. Bao, R. Zhang, G. Enemali, Z. Cao, B. Zhou, H. McCann, and C. Liu, "Relative Entropy Regularized TDLAS Tomography for Robust Temperature Imaging," *IEEE Transactions on Instrumentation and Measurement,* vol. 70, pp. 1-9, 2021.

[33] N. Polydorides, A. Tsekenis, E. Fisher, A. Chighine, H. McCann, L. Dimiccoli, P. Wright, M. Lengden, T. Benoy, D. Wilson, G. Humphries, and W. Johnstone, "Constrained models for optical absorption tomography," *Applied Optics,* vol. 57, no. 7, pp. B1-B9, 2018.

[34] T. Yu, and W. Cai, "Benchmark evaluation of inversion algorithms for tomographic absorption spectroscopy," *Applied Optics,* vol. 56, no. 8, pp. 2183-2194, 2017.